Chapter 3.　　Collider Accelerator Physics and Design

3.1　Two Colliders in One Tunnel

3.1.1　Footprint Issues

For the design study it has been envisioned that the Low Field (LF) ring will be comprised of long, combined function magnets—the bending of the central trajectory and the focusing of the particle beam will be performed using gradient magnets with central field strength on the order of 2 T. The High Field (HF) ring will use separated function magnets—dipole magnets for bending the central trajectory and quadrupole magnets for focusing. Since the LF and HF designs have different focusing characteristics, the dispersion suppressors must also be designed simultaneously to ensure that the LF and HF orbits line up appropriately when entering the long straight sections for the Interaction Regions and Utility Regions.

As stated earlier, the size of the arcs is determined primarily by the low magnetic field of the first stage collider, while the lengths of the major straight sections are determined by the high magnetic rigidity of the beam in the second stage collider. The interaction regions must be made long enough to accommodate trajectory and optics manipulations of high energy proton beams using reasonable guesses for sizes of future high energy, high luminosity detectors. The utility straight section regions must be made long enough to provide space for extracting a very high energy proton beam toward a beam dump and for beam scraping and beam instrumentation at high energy. All of these functions will be required for the LF collider as well, of course, but the technologies used for injection, extraction, acceleration, and so forth will be similar for the two rings. Thus, the requirements of the HF design will set the scale for the straight sections.

3.1.2　Optics Issues

In addition to the geometric layout of the two rings, many optical properties must be decided simultaneously as well. The Low Field ring uses gradient magnets in the arcs of the collider, while the High Field ring uses quadrupole FODO cells. For simplicity of instrumentation, power distribution, cable runs, etc., it is desirable for the maximum beam size locations in the HF arc to correspond with those in the LF arc. Dispersion suppressor regions typically are made by reducing the total bending in two consecutive cells by half. The proportion of bending to leave out in each of the cells depends upon the phase advance per cell. In combined function lattices, such as the LF design, the bending magnets also provide focusing, so this tactic must be modified. While combined function designs of dispersion suppressors have been performed in the past (e.g., Fermilab Recycler), the choice of cell phase advance and cell lengths must be settled upon for both rings to ensure a consistent dispersion suppressor design. (Obviously, this is an issue for both optics and geometry as well.) This is another reason that it was chosen to give the two colliders equal cell lengths and equal betatron phase advances per cell. Each collider, LF and HF, is made of two separate, but linked, accelerators. The choice must be made as to whether adjacent magnets have the same or opposite focusing characteristic with respect to each other for the beam traveling through them. This affects the matching of sections

going into and out of straight sections, as well as the design of the beam transfer system joining the LF and HF rings. The decision must be made in coordination with the magnet design effort. Finally, the magnet choice for the LF collider is a horizontally separated two-in-one iron dominated magnet. To ensure that the two beam trajectories have the same path length, the beams will need to be crossed several times about the circumference. Space and optical designs must be incorporated into the layout to accommodate this feature. The two beams of the high field collider are naturally separated vertically in the common coil arc magnets.

3.1.3   Approach to Design

As indicated in Figure 3.1 each collider is made up of two major arcs that connect two clusters of straight sections. At the outset, only one cluster region—located at or near the Fermilab site—will be equipped with full interaction region and utility region optics. The opposite cluster will have the same straight section lengths, but optically will consist of simpler, FODO-type modules where applicable, with the exception of a special straight section designs to accommodate beam scraping and future beam transfers between the LF and HF accelerators.
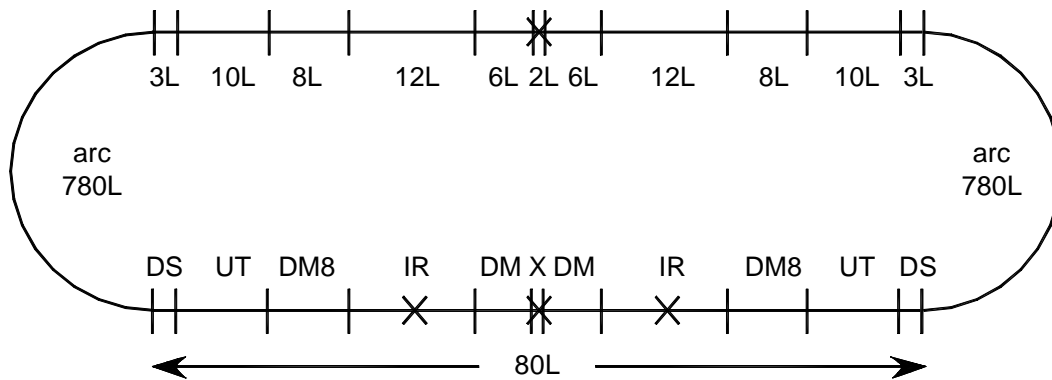

Figure 3.1. Schematic layout of collider modules. The figure is not to scale, emphasizing the straight section functions.

Dispersion suppressor modules are adopted following the SSC design, which was also later used in the Fermilab Main Injector. A cell phase advance of 90 degrees has been chosen for which a dispersion suppressor can be made using two special cells, each 3/4 the length of a standard cell and each containing 2/3 the bending of a standard cell. These modules reduce the periodic arc dispersion function to zero at the output of two such cells. The short bending regions between Interaction Regions and Utility Regions will be composed of back-to-back dispersion suppressor modules. Any additional bending required in these regions is generated by inserting standard half-cells between the DS modules.

3.1.4   Footprint Parameters

Table 3.1 lists the fundamental parameters of the footprint. In the transition from Stage-1 to Stage-2 operation, the experiments will remain centered on the same interaction points. At the same time it is envisaged that they will be upgraded to take up more space along the beam line, increasing the distance from the IP to the first magnet, L^*, from 20 to 30 m. It is therefore

necessary to allow for a bypass to keep the low field ring beams well clear of the experiments. This must be done without changing the total low field ring circumference.

One advantage of modular construction is that low and high field lattices are guaranteed to have almost identical footprints, and therefore to fit in the same tunnel, so long as corresponding low and high field modules are placed on top of each other. The maximum deviation is only a few millimeters, easily allowing one ring to be placed on top of the other at all locations in the VLHC tunnel.

Table 3.1. Fundamental lattice parameters common to both low and high field rings.

Circumference, C	233.037	km
Average arc radius, R	35.0	km
Number of interaction points	2	
Half cell length, L_{hc}	135.486	m
Half cell bend angle, q_{hc}	3.875	mrad
Half cell count	1720	
Half cell harmonic, n_1	24	
Bunch spacing (53.1 MHz), S_B	5.645	m
Time between bunches	18.8	ns
Number of buckets	41280	
Number of bunches, M	37152	
Phase advance per cell	90.0	deg
Revolution frequency	1.286	kHz
Revolution period, T	0.778	ms
Harmonic number, h	371520	
RF frequency (9 x 53.1)	478.0	MHz

3.1.5   Half-cell Length

The average bending radius of the arcs is made as close as possible to the goal value of $R = 35$ km by adjusting the total equivalent number of (bending) arc cells in each ring. Each of the 4 short half-cells in each dispersion suppressor has 2/3 the bending of an arc half-cell. Thus, the 20 dispersion suppressors (on either side of 10 straights) have a total bending equivalent to 160/3 arc half-cells. If there are $N = 784$ arc half cells in each half of the VLHC, then the bend per half cell is

$$q_{hc} = \frac{2p}{2N + 160/3} = 3.875 \text{ mrad}$$ Eq. 3.1

and the average arc bend radius is

$$R = \frac{L_{hc}}{q_{hc}} = 34.961 \text{ km}$$ Eq. 3.2

The (minimum) bunch spacing S_B is taken to be one 53.1 MHz RF wavelength in the Tevatron

$$S_B = l_{53} = \frac{(2000 \text{ m})p}{1113} = 5.645 \text{ m}$$ Eq. 3.3

This guarantees that the filling schemes from the Tevatron will be relatively simple. The bunch time spacing of about 18.8 ns is not unreasonably challenging to the experiments.

The half-cell length is

$$L_{hc} = n_1 S_B$$
<div align="right">Eq. 3.4</div>

The bunch spacing can trivially be increased (for example during commissioning) by any of the common factors of the "half cell harmonic number" n_1. The value of $n_1 = 24$ was chosen for both low and high field rings, corresponding to a half-cell length of $L_{hc} = 135.4865$ meters.

This half cell length is short enough to keep the natural horizontal emittance due to synchrotron radiation in the high field ring, $e_{nat} = 0.04$ μm, much smaller than the horizontal emittance $e_x \approx 0.20$ μm which must be maintained (by heating) to avoid beam-beam limits in the store. A stronger limit to the maximum arc half-cell length is the need to limit the vulnerability of the low and high field rings to systematic field harmonic errors in the arc bending magnets. This is more critical for the low field ring, simply because the injection energy is an order of magnitude lower (1 TeV) than for the high field ring (10 TeV).

The current value of $L_{hc} = 135.4865$ m is by no means fully optimized, not least because we do not accurately understand what values of systematic magnet harmonics might be achieved in industrial production of the arc bending magnets.

3.2   Stage 1 – the Low Field Ring

The first stage low-field collider will have a top energy of 20 TeV and peak (initial) luminosity of 10^{34} cm^{-2}sec^{-1}. The collider will use the Tevatron as its injector operating at a transfer energy of 900 GeV. For this study a transverse emittance of 1.5 π mm-mrad (rms, normalized) is used, which is typical for the Fermilab Booster, though about half the value at the Tevatron under recent normal operations. It is anticipated that with further Run II experience, the efficiency of emittance preservation will increase. Using the present acceleration systems of the Tevatron injector chain, the collider has a bunch spacing of 5.645 m (53.1 MHz), which sets the number of available RF buckets. With a 90% filling fraction to allow for gaps in the beam for various kicker rise times, the number of protons per bunch required in the Stage-1 collider is approximately 2.6×10^{10}, similar to Tevatron bunch intensities during previous Fixed Target operations. Using an interaction region design with a $b^* = 0.3$ m, we arrive at the desired initial luminosity. Table 3.2 lists the general parameters of the Stage-1 collider.

The typical store parameter evolution is depicted in Figure 3.2. The figure shows the proton bunch intensity and luminosity decreasing due to collisions. The vertical emittance also decreases slightly due to synchrotron radiation damping which occurs with a damping time of about 100 hr. Due to the use of gradient magnets in the Stage-1 collider the horizontal emittance actually will be *anti-damped*, and will increase at approximately the same rate. This should not be a problem since store times will be much less than 100 hours.

Table 3.2. Nominal store parameters for the low field collider.

Storage energy	20	TeV
Peak luminosity	10^{34}	$cm^{-2}sec^{-1}$
Packing fraction	89	%
Injection energy	0.9	TeV
Transverse normalized emittance, rms (H&V, inject)	$1.5\,\pi$	μm
Initial bunch intensity	2.6×10^{10}	
Average beam current	195	mA
Stored energy per beam at collision	3.0	GJ
Bend field at storage	2.0	T
Bend magnet gradient	9.0	T/m
Phase advance per cell	90.0	deg
Max rms arc beam size (inject)	1.2	mm
Bunch spacing (53.1 MHz)	5.645	m
Time between bunches	18.8	nsec
Bunch length	30	mm
Longitudinal emittance, rms (inject)	0.4	eV-s
RF voltage at storage	50	MV
Fill time	60	min
Acceleration time	1000	sec
Beam size (rms) at IP (storage)	4.6	μm
Total crossing angle (10s separation in drift space)	153	μrad
Distance from IP to first magnet	21	m
b^{*} at IP (H & V)	0.3	m
Maximum interactions per crossing	20	
Debris power at IP (each direction)	3	kW
SYNCHROTRON RADIATION AT STORE		
Energy loss per turn per particle	38	keV
Radiation damping time, t_0	100	hr
(anti-damping in H plane)		

3.2.1   Lattice

The bulk of the lattice is characterized by its construction from just three optical building blocks—arc, dispersion suppressing, and straight-section cells. The arc and suppressor cells consist of combined function gradient magnets and have space allocated at maximum-b sites for 4 correction elements. Additional corrector space is available at the quarter-cell locations ($b_x = b_y$) for lumped correction of systematic multipoles [1]. Two utility straights, each of which must accommodate 900 GeV injection from the Tevatron plus abort of 20 TeV beams are needed. The beams collide with a horizontal crossing angle at two interaction points where $b^{*} = 30$ cm. In a special cell, midway between the IP's, the beams are made to cross over

between the inner and outer horizontal apertures. Diametrically opposed in the ring, a mirror of this cell is installed to ensure identical path lengths for the two circulating beams.
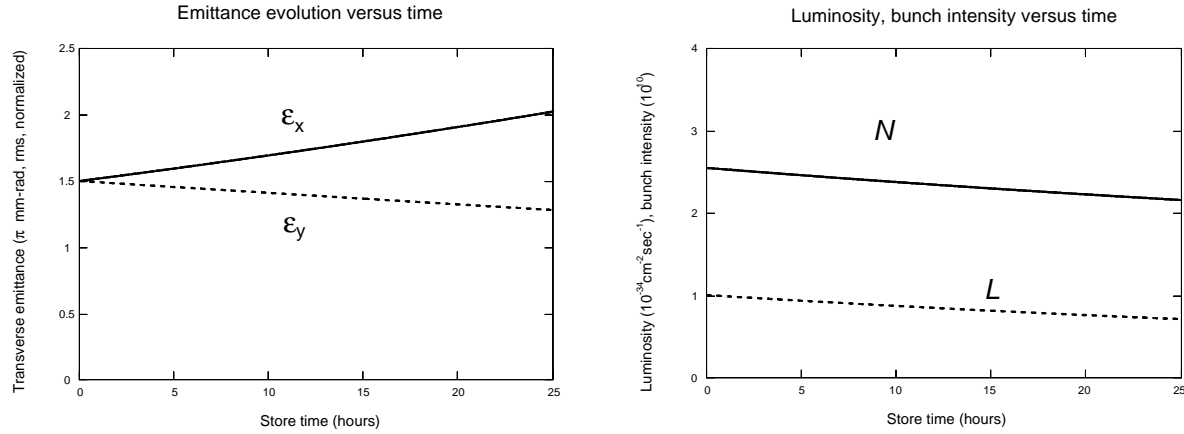

Figure 3.2. Evolution of collider parameters during a typical store.

3.2.1.1 *Interaction Regions*

The final foci in the IRs are anti-symmetric triplets, formed from single-bore, 300 T/m magnets. Four additional quadrupole circuits, comprising double-bore, 70 T/m magnets, are also used in optical matching. With a total of 6 independently-tunable quadrupole circuits available it is possible to match the four β's and α's from the IP to regular FODO cells, and hold the phase advance $\Delta\mu$ constant across the IR through the squeeze from $\beta^* = 6.00$ m $\rightarrow 0.30$ m. Fixing $\Delta\mu$ eliminates the necessity of a special phase trombone to maintain the nominal operating point. Figure 3.3 shows the lattice functions through the IR during collisions.

The circulating beams are separated horizontally by 15 cm throughout the arcs and 70 T/m straight-section quads. Four dipoles, 13.6 m each at 1.97 T, situated between the Q3 and Q4 quadrupoles bring the beams together at the entrance to the triplet for collisions at the IP. Dipoles downstream of the IP separate the beams again and channel them back into the inner and outer rings. A half-crossing angle of 77 µr at the IP gives 10σ separation between the beams at the first parasitic crossing.

3.2.1.2 *Injection and Abort Straight Sections*

To accommodate 900 GeV injection from the Tevatron, as well as 20 TeV proton abort, 5 straight-section cells are modified as shown in Figure 3.4. The long drift space (377 m) created by triplet focusing produces sufficient room for abort Lambertsons (see Section 5.1.5.4) and beam extraction.

Dipoles separate the circulating beams through the utility straight to make room for RF cavities downstream of the second triplet. Three 21.54 m dipoles at 2 T bend the beams apart by 40 cm, followed immediately by 3 more dipoles that flatten out the trajectories. This pattern is reversed downstream of the RF to bring the beams back into standard double-bore magnets.
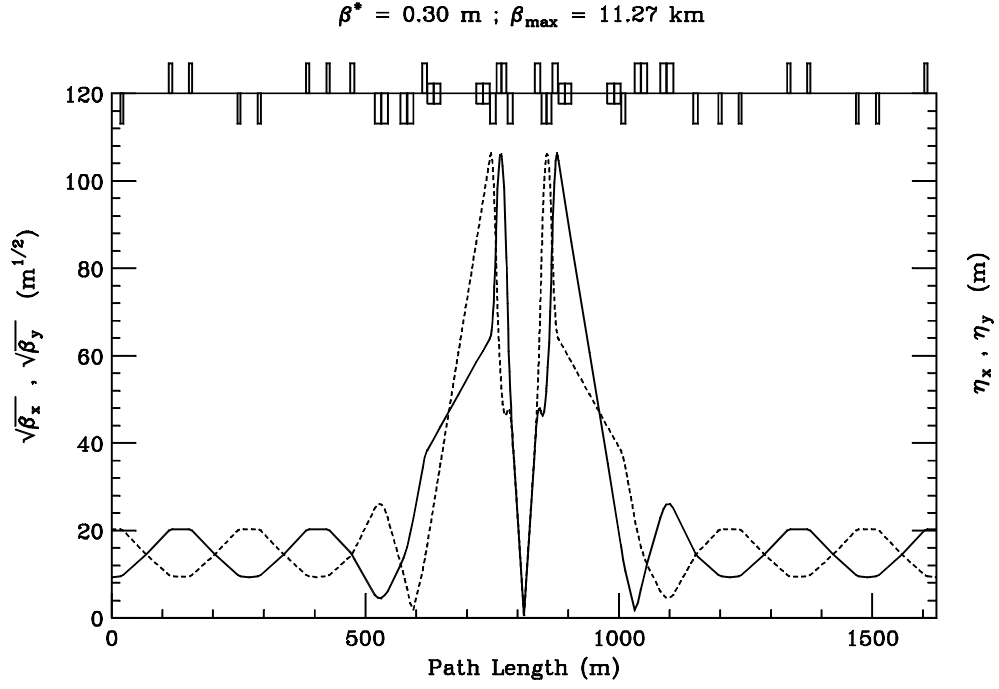
$\beta^* = 0.30 \text{ m} \; ; \; \beta_{\text{max}} = 11.27 \text{ km}$

Figure 3.3. IR lattice functions in the collision configuration.
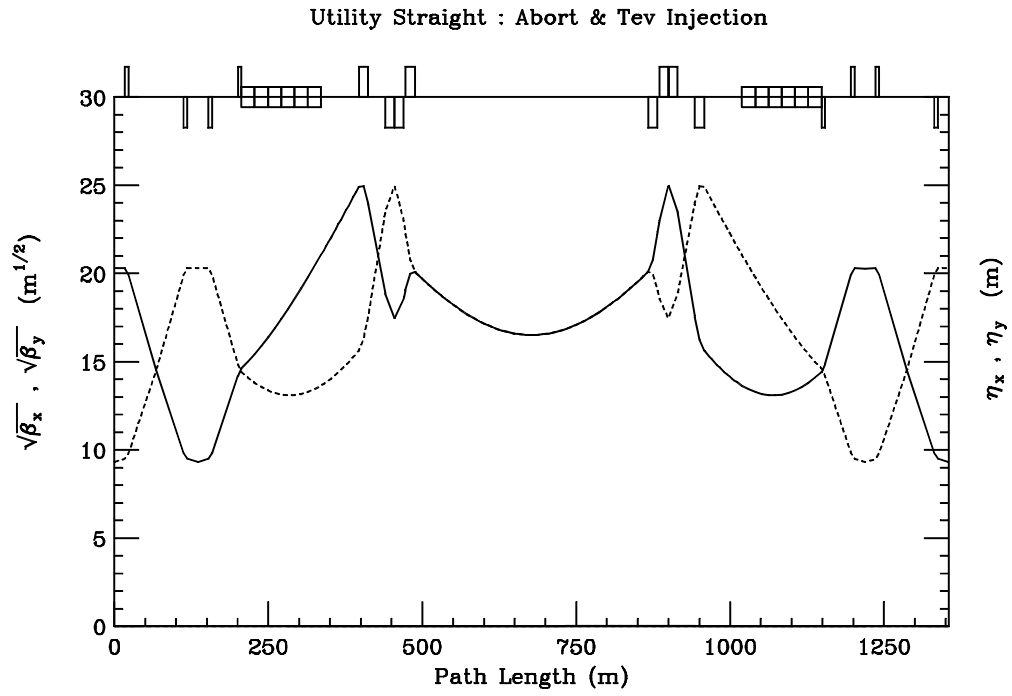
Utility Straight : Abort & Tev Injection

Figure 3.4. Layout of a utility straight supporting beam transfer from the Tevatron and 20 TeV abort. (See Section 5.2.5.4.)

3.2.1.3   Beam Crossovers

With the beams separated horizontally in the arcs it is necessary to move the beams between the inner and outer rings to maintain identical path lengths. In the LF ring 2 crossover cells are inserted on opposite sides of the ring. Four rolled dipoles move the beams the 15 cm from one channel to the other. Each dipole is 36 m at 1.944 T. The first dipole is rolled by 0.12 rad to start separating the beams vertically, while bringing them closer together horizontally. The second bend is rolled by −0.12 rad to flatten the vertical trajectory. At the crossing point the beams are separated vertically by 9 mm. This is 17.8σ at the injection energy of 900 GeV. Rolled dipoles after the crossing point remove the vertical offsets and complete the 15 cm transverse transfer of beams to the opposite channel.

3.2.1.4   Miscellaneous Insertions

For momentum collimation a localized dispersion wave is generated in a 5-cell straight section (Figure 3.5). Four 45 m dipoles (2 T @ 20 TeV) at the upstream end of the straight move the beams transversely by 0.36 m, creating ±70 cm of dispersion. Four more dipoles downstream bring the beams back onto their nominal trajectory and cancel the dispersion.

Free space for damping systems, beam instrumentation, etc. (see, for example, Figure 5.53) can be generated by replacing standard arc gradient magnets with a shorter, modified version plus a small quadrupole. Through this insertion, the β's, α's, and phase advance of an arc cell are exactly reproduced by a gradient magnet with $B' = 9.185$ T/m (1% weaker than the regular arc magnets) plus a 2.0 m quadrupole with $B' = 26.14$ T/m. The low field of the quadrupole makes it just a longer version of the normal arc trim quads. The dispersion wave created by the holes is cancelled locally with 90° of phase advance per cell.
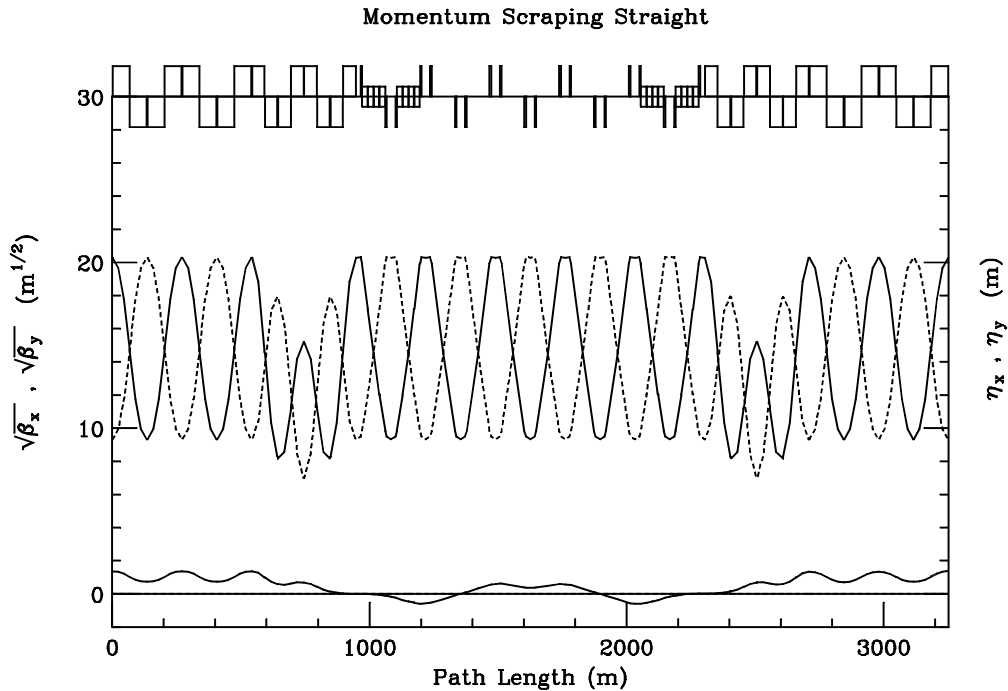

Figure 3.5. Dispersion creation in a 5-cell straight for collimation.

3.2.2   Magnet Apertures and Field Quality

The available mechanical aperture determines the required dynamic aperture. Collimators define the limiting aperture in most cases and they are usually placed at around 6σ from the center of the beam pipe. This allows 3σ for the beam distribution, and another 3σ for injection errors and orbit drifts over time. The real dynamic aperture therefore must be greater than 6σ in order to avoid significant losses of particles at places in the ring outside the beam cleaning section.

Errors, time dependent fields and other imperfections in a real machine can never be modeled accurately enough in a simulation, so the dynamic aperture calculated by a simulation always exceeds the measured dynamic aperture. Observations at the Tevatron, HERA, and SPS have shown that the agreement between the measured and calculated dynamic aperture varies between 20-100%. As a consequence the LHC, for example, requires that the calculated dynamic aperture after 10^5 turns at both injection and collision (with only magnetic non-linearities) equal 12σ. Since the errors listed above are just as likely for the VLHC, it seems reasonable to adopt a dynamic aperture requirement of 12σ after 10^5 turns.

3.2.2.1   Scaling the Main Injector Errors

As a starting hypothesis, the errors in the Main Injector are used as a scaling basis, assuming that the mechanical errors scale with the pole tip gap. Thus we assume that the field errors in the VLHC low field transmission line magnets at a pole tip radius of 10 mm are the same as the errors in the Main Injector magnets at a pole tip radius of 1 inch. The bend fields in the Main Injector at 8 GeV and in the VLHC at an injection energy of 1 TeV are nearly the same: $B_0^{MI} =$ 0.101 T, $B_0^{VLHC} = 0.098$ T.

We make the somewhat stronger assumption that the equality is satisfied for every harmonic n so that we obtain the following scaling relation between the multipole coefficients in the Main Injector and those in the VLHC,

$$\left[\frac{b_n}{R_{ref}^n}, \frac{a_n}{R_{ref}^n}\right]^{VLHC} = (2.54)^n \times \left[\frac{b_n}{R_{ref}^n}, \frac{a_n}{R_{ref}^n}\right]^{MI} \qquad \text{Eq. 3.5}$$

*Table 3.3. Systematic <> and random **s** of multipole coefficients used for the VLHC, scaled from Main Injector magnets using Equation 3.5. The coefficients are shown in units of 10^{-4} at a reference radius of 10 mm.*

Order, n	$<b_n>$	$<a_n>$	$s(b_n)$	$s(a_n)$
2	-0.600	0.000	0.600	0.200
3	0.000	0.000	0.149	0.300
4	0.300	0.000	0.300	0.150
5	0.000	0.000	0.100	0.500
6	0.000	0.000	0.250	0.250

Table 3.3 shows the derived harmonics for the low field magnets. We have assumed that the measured systematic skew harmonics in the Main Injector magnets are the result of the top

down asymmetry in the magnet bus work [2]. This should not be an issue for the low-field magnets since the bus work is symmetric, and so the nonlinear skew harmonics have been set to zero.

3.2.2.2   *Dynamic Aperture at Injection*

The main issue is to determine whether the field quality is good enough to meet the target set for the acceptable dynamic aperture. If not, a nonlinear corrector system that increases the dynamic aperture to the target value must be developed. The results shown below will be refined at a later stage when more information on the field quality is available. For most calculations reported here, particles are tracked for 1024 turns without synchrotron oscillations in a perfectly aligned lattice. The only nonlinearities are the chromaticity sextupoles and the field errors in the arc magnets. Sources of coupling are not introduced so correction with skew quadrupoles is not necessary. The fractional tunes are set to the Tevatron values $v_x = 0.581$, $v_y = 0.575$.

The impact of linear coupling is reduced when there is a difference in horizontal and vertical integer tunes. In the perfect aligned lattice there are no sources of linear coupling. Nevertheless the influence of tune splits on the dynamic aperture for the cases $\boldsymbol{n}_x$- $\boldsymbol{n}_y = \pm 2, \pm 4, \pm 6$ were studied. In no case did the dynamic aperture improve and in some cases the aperture was reduced significantly, presumably due to the beta beating.

Figure 3.6 shows the dynamic aperture with only chromaticity sextupoles, only random errors, only systematic errors and all the errors. The dynamic aperture with all errors is nearly the same as that with only the random errors. Tracking with all the field errors at injection shows that the dynamic aperture is about 20σ as shown in Table 3.4. Increasing the number of turns to 100,000 typically results in a decrease of the dynamic aperture by about $2\text{-}3\sigma$. This suggests that the target dynamic aperture of 12σ at 100,000 turns should be met with this set of assumed errors.

3.2.2.3   *Dynamic Aperture at Collision*

The dynamic aperture at collision optics will be dominated by the field errors of the IR quadrupoles due to the large beam sizes in these magnets. The IR quadrupoles with their high gradients will be built with "conventional" superconducting magnets. The nonlinear harmonics in these magnets are well understood following decades of development and also through the Fermilab program of building these quadrupoles for the LHC. The errors in the arc magnets built with conventional technology usually are not significant in determining the dynamic aperture at top energy. For example, the target dynamic aperture in the LHC at top energy is set at 12σ with only the IR quadrupole field errors. We will adopt the same target dynamic aperture of 12σ in the simulations.

Dynamic Aperture of VLHC Low Field Lattice

At injection energy, nuX=0.581, nuY=0.575, RMS emittance 1.5 pi

Legend:
- With only chromaticity sextupoles (CS)
- With CS & random errors
- With CS & systematic errors
- With CS & random & systematic errors

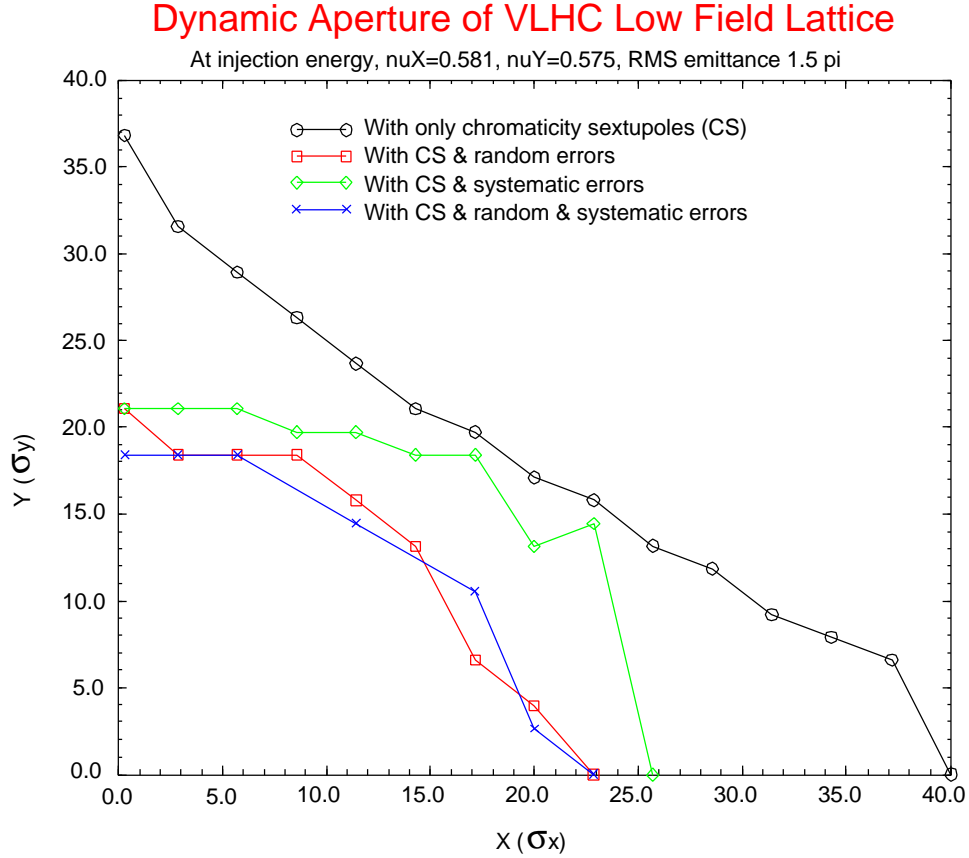X axis: $X\ (\sigma_x)$
Y axis: $Y\ (\sigma_y)$

Figure 3.6. Dynamic aperture at injection with only chromaticity sextupoles(CS), CS and random errors only, CS and systematic errors only, and CS with all errors. The target dynamic aperture is 12σ.

Table 3.4. Dynamic aperture at injection energy with various sets of errors in the arc magnets. These results show that the random errors together have a somewhat larger impact on the dynamic aperture than the two systematic components $<b_2>$, $<b_4>$. The dynamic aperture with all the errors is about the same (20σ) as without the systematic errors.

Errors	Dynamic Aperture	
	Average	Minimum
Only chromaticity sextupoles (CS)	30.9	25.4
CS and only random errors	20.0	18.4
CS and only systematic errors	23.4	21.1
CS and all errors	19.7	18.4
CS and only random errors and $\sigma(b_2)=\sigma(a_2)=0$	20.4	18.6
CS and only random errors and $\sigma(b_3)=\sigma(a_3)=0$	20.2	17.6
CS and only $<b_2>\neq0$	31.5	25.2
CS and only $<b_4>\neq0$	24.5	21.1

The arc magnets in the Stage-1 collider, however, are built with transmission line magnets, which have different characteristics from conventional superconducting magnets. At high current, the field in the iron saturates leading to a drop in the gradient and a large negative sextupole component (b_2). While quadrupole correctors in every cell to maintain the correct

phase advance per cell will compensate the change in gradient, the compensation of the sextupole component is a more serious issue. If the nonlinear fields due to magnet saturation have a significant impact on the dynamic aperture, then this could potentially limit the maximum energy reach of the low field collider.

The straightforward approach to compensating the saturation b_2 component is to use the chromaticity sextupoles in the cells to correct the linear chromaticity. At large $|b_2|$ this leads to strong chromaticity sextupoles lumped at two locations in the cell, one SF next to the focusing magnet (F), the other SD next to the defocusing magnet (D). A calculation of the dynamic aperture at 20 TeV without the IR errors but with the b_2 component in the arc magnets due to saturation shows that the dynamic aperture is quite large even up to 10 units of b_2. At $b_2=0$, integrated strengths required for the F and D type sextupoles are (946, 1761) T/m respectively. At positive b_2 £ 3, the F sextupoles decrease and D sextupoles increase in magnitude and vice versa at negative b_2 ³ -3. At larger absolute values of b_2, both sextupole strengths increase in magnitude. If required, additional sextupoles could be placed in the 1 m gap between the F and D and the D and F magnets to correct the chromaticity generated by the iron saturation. This would lower the integrated sextupole strengths and allow for larger values of b_2 to be compensated.

The impact of magnet saturation should, however, be determined in the presence of the dominant field errors of the IR quadrupoles. We have based our dynamic aperture calculations on the expected field errors calculated by G. Ambrosio et al. [3].

The dynamic aperture was calculated for three seeds for the random errors with the signs of the uncertainties in the systematics alternating between positive and negative. The random errors were truncated at 3σ. For each seed the dynamic aperture was calculated with $-10 \leq b_2 \leq 10$. At $b_2 = 0$, the dynamic aperture drops to around 20σ in the presence of the IR errors, compared to a value of around 130σ without these errors but only chromaticity sextupoles. The average dynamic aperture varies over a small range of 20-23 σ when $b_2 \leq 10$. Clearly the saturation sextupoles do not have a significant impact on the dynamic aperture at 20 TeV. The maximum tolerable value of b_2 may instead be limited by the sextupole strengths required to correct the chromaticity.

3.2.2.4   *Dynamic Aperture with Synchrotron Oscillations*

After correction of the orbit due to misaligned magnets, the rms closed orbit deviations were reduced to $<x>_{rms} = 0.22$ mm, $<y>_{rms} = 0.21$ mm. The fractional tunes were $n_x = 0.585$, $n_y = 0.573$. Figure 3.7 shows the average and minimum dynamic aperture with synchrotron oscillations and closed orbit errors as a function of the momentum deviation amplitude. The average and minimum are taken over three random seeds. The average dynamic aperture at $dp/p = 0$ is $19s$ while at $dp/p = 3 \times 10^{-4} \approx 3s_p$, the average dynamic aperture drops to about $11s$ which is only slightly under the target value.
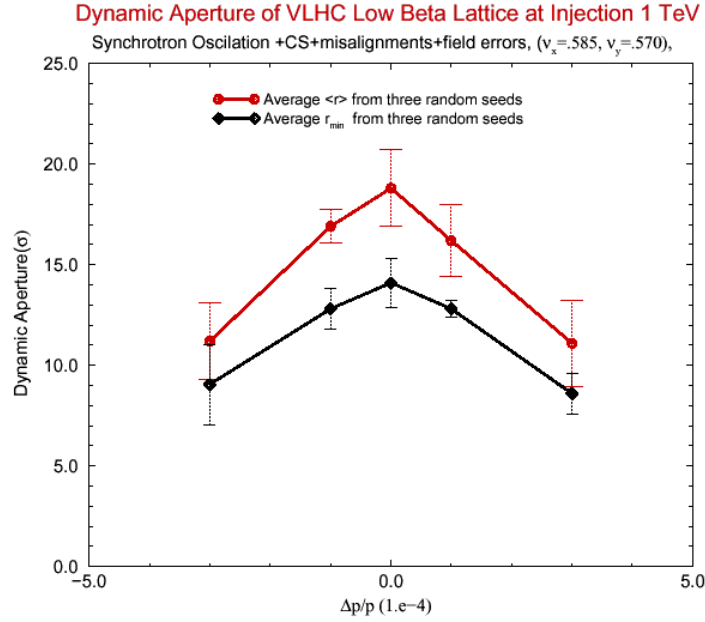
Figure 3.7. Dynamic aperture with synchrotron oscillations and closed orbit errors. Particles were tracked for 10,000 turns and with three random seeds.

3.2.3   Tolerances and Corrections

3.2.3.1   *Closed Orbit*

Distortions of the ideal closed trajectory in the collider will be primarily generated by transverse alignment errors. The trajectory in the horizontal plane will also be influenced by errors in the main bend field of the magnets, and the vertical trajectory will be further distorted due to roll errors in the main bending field.

For a bending magnet of length L with gradient B' which is displaced transversely from its ideal position by an amount d, a particle with magnetic rigidity $B\boldsymbol{r} = p/e$ will have its trajectory deflected through an angle $\boldsymbol{q} = (B'L/B\boldsymbol{r})\,d$. For the low field collider, the gradient magnets have lengths roughly equal to the half-cell length and will be supported along its length by several adjustable magnet stands. If the arc magnets are divided into n equal-length sections for support and alignment, then the rms expected closed orbit deviations in the horizontal (x) and vertical (y) degrees of freedom at maximum β locations in the arcs are given by

$$\Delta\widehat{x}_{co} = \frac{\sqrt{\widehat{b}\langle b\rangle}}{2|\sin \boldsymbol{pn}|}\sqrt{\frac{N}{2}}\left(\frac{B_0 L}{B\boldsymbol{r}}\right)\sqrt{\frac{1}{n}\left(\frac{B'd_{rms}}{B_0}\right)^2 + \left(\frac{\Delta B}{B_0}\right)^2_{rms}} \qquad \text{Eq. 3.6}$$

and

$$\Delta\widehat{y}_{co} = \frac{\sqrt{\widehat{b}\langle b\rangle}}{2|\sin \boldsymbol{pn}|}\sqrt{\frac{N}{2}}\left(\frac{B_0 L}{B\boldsymbol{r}}\right)\sqrt{\frac{1}{n}\left[\left(\frac{B'd_{rms}}{B_0}\right)^2 + \boldsymbol{f}^2_{rms}\right]} \qquad \text{Eq. 3.7}$$

where $(DB/B_0)_{rms}$ is the rms field strength deviation of the full magnet, d_{rms} is the rms displacement of the magnet sections, and f_{rms} is the rms roll angle (with respect to vertical) at the n locations within a half-cell. N is the number of half-cells in the collider.

For typical values of the above variables we use $n = 5$ over a half cell length of $L = 67$ m, $b_{max} = 411$ m, $<b> = 250$ m, $B_0 = 2$ T, $B' = 9$ T/m, $d_{rms} = 250$ μm, $f_{rms} = 0.5$ mrad, and $(DB/B_0)_{rms} = 10^{-4}$. From a distribution of errors over the 780 arc cells in the collider, we obtain expected rms orbit errors on the scale of

$$\Delta \widehat{x}_{co} \approx 9.5 \; mm \qquad\qquad\qquad \text{Eq. 3.8}$$

$$\Delta \widehat{y}_{co} \approx 10.3 \; mm \qquad\qquad\qquad \text{Eq. 3.9}$$

The maximum uncorrected closed orbit excursions clearly venture outside any reasonable beam pipe radius.

To correct the orbit distortions, we assume dipole correctors are placed at maximum b locations in the arcs (H & V), and a standard 3-bump algorithm is performed. The corrector strength necessary to perform the correction using the parameters introduced above would be

$$\Theta_x = \frac{\sqrt{2}}{\sin m} \sqrt{\frac{\langle b \rangle}{\widehat{b}}} \left(\frac{B_0 L}{Br} \right) \sqrt{ \frac{1}{n} \left(\frac{B' d_{rms}}{B_0} \right)^2 + \left(\frac{\Delta B}{B_0} \right)^2_{rms} } \qquad\qquad \text{Eq. 3.10}$$

and

$$\Theta_y = \frac{\sqrt{2}}{\sin m} \sqrt{\frac{\langle b \rangle}{\widehat{b}}} \left(\frac{B_0 L}{Br} \right) \sqrt{ \frac{1}{n} \left[\left(\frac{B' d_{rms}}{B_0} \right)^2 + f^2_{rms} \right] } \qquad\qquad \text{Eq. 3.11}$$

where m is the cell phase advance. For $m = 90°$, and the same parameter values as before, the rms corrector strengths are

$$\Theta_x \approx 2.3 \; mrad \qquad\qquad\qquad \text{Eq. 3.12}$$

$$\Theta y \approx 3.2 \; mrad \qquad\qquad\qquad \text{Eq. 3.13}$$

At 20 TeV, a 3 μrad bend angle requires an integrated field strength of 0.2 T-m. To be able to correct at the 2.5-σ level, steering correctors should have strengths of approximately 0.5 T-m. The maximum corrector strengths will be dominated by displacement errors caused by diffusive ground movement and ground settlement over time.

3.2.3.2   Quadrupole Effects

The quadrupole gradient in the transmission line magnets drops steeply at high fields due to saturation of the iron. Quadrupole correctors, one in each plane, will be placed in every arc cell to maintain the required phase advance of 90° per cell. At present these correctors are 0.5 m long and placed at the beginning of each half-cell. The correctors, independently powered, have been sized to correct the gradient shift due to magnet saturation at 2 Tesla.

Sources of errors in the tune include gradient errors and closed orbit distortions in the non-linear magnets. Quadrupole correctors in the arcs will be used to control the global tunes and to split the integer tunes to reduce the sensitivity to systematic linear coupling sources.

It will be important to restrict the beta beating to a low value everywhere, both for on-momentum and off-momentum particles. It will be especially important to isolate the interaction regions from beta-beating errors generated elsewhere in the ring. Quadrupoles at the entrances and exits of the arcs and at the entrances and exits of the straight sections can be used to control both the amplitude and phase of $\Delta\beta/\beta$.

Normal quadrupole gradient errors and skew quadrupole gradient errors will contribute to horizontal and vertical dispersion beating respectively. The errors generated in the arcs and utility straight sections will be corrected either by quadrupole correctors or by the closed orbit correctors. It will be important to keep the dispersion at the IPs very small. Local dispersion correction within the IRs will be necessary to correct the dispersion generated by the crossing angle.

3.2.3.3   *Coupling*

Sources of coupling include skew quadrupole errors in the main magnets, rolls of the gradient magnets and vertical orbit distortion through the nonlinear magnets. Requiring that the minimum tune split be less than 0.05 before correction may set the tolerance for the allowed coupling. Larger values make coupling correction with skew quadrupoles difficult.

Skew quadrupoles placed in regions of horizontal dispersion will generate vertical dispersion, which will need additional correction. It is therefore preferable to place these quadrupoles in straight sections. Two families of skew quadrupoles in the utility straight sections and the IRs will be sufficient to control the effects due to the difference resonance $\boldsymbol{n}_x - \boldsymbol{n}_y = p$. These families will be placed so that the difference in phases $\boldsymbol{y}_x - \boldsymbol{y}_y$ differs by $\boldsymbol{p}/2$ at the families. The coupling sum resonance $\boldsymbol{n}_x + \boldsymbol{n}_y = p$ may also need to be corrected (depending on the strength of the skew quadrupole errors). In this case an additional two families will be required, placed so that $\boldsymbol{y}_x + \boldsymbol{y}_y$ differs by $\boldsymbol{p}/2$ at these families.

3.2.3.4   *Chromaticity Effects*

The linear chromaticity is controlled by two families of sextupoles, one in each plane, placed in every arc cell. These families can be defined in software, since all correctors are independently powered, as described in Section 5.2.3. This will suffice provided the nonlinear change of tune with momentum is small over the required momentum aperture. If the global nonlinear chromaticity requires correction, then two families of sextupoles in each plane for the 90°cells will be required. It would therefore be desirable to place sextupoles (of say the F type) in every other cell on one bus and the other family of sextupoles in the other cells on another bus.

In addition to the chromaticity due to the quadrupoles, there is a contribution due to sextupole fields caused by iron saturation at fields close to 2 Tesla. This chromaticity must also be compensated by the chromaticity sextupoles. This has been discussed in the section on the dynamic aperture at collision.

If the beta function is strongly dependent on the momentum, then it can lead to an increased spot size if not corrected at the IPs and to emittance growth due to injection errors if not corrected at the injection point. Correcting the momentum dependence of the beta functions will require additional sextupole families.

For the IRs, a local chromaticity correction system was proposed for the SSC [4], which increased the momentum aperture from about 2.5σ with linear chromaticity correction to about 8σ with correction of the nonlinear chromaticity generated by the IRs. A similar system may be required for the IRs if the momentum aperture needs to be increased.

3.2.3.5   *Alignment Tolerances in the IRs*

These tolerances are more stringent for the IR quadrupoles than for any other magnets in the ring. Several criteria have to be met including:

- Dispersion at the IP should be small, both to attain maximum luminosity and to avoid synchro-betatron resonances.

- Beam excursions in the triplets should be limited to preserve the dynamic aperture.

- Separations between the beams at the parasitic collision points should not decrease.

In the IR quadrupoles the beta functions change rapidly and are not symmetric about the quadrupole center. As a consequence, pitch and yaw misalignments will introduce substantial beam separations at the IPs if not corrected. Due to the crossing angle a roll misalignment of an IR quadrupole will introduce orbit shifts in the plane orthogonal to the crossing plane. This is in addition to the extra coupling generated by the roll angle. Thus misalignments in all six degrees of freedom of these IR quadrupoles need to be well controlled and corrected.

Orbit offsets at the IPs

The orbit offset at the IP $z_{offset}(IP)$ due to a transverse displacement $\boldsymbol{D}z_Q$ of an IR quadrupole (assumed to be at 90 degrees from the IP) is

$$\frac{z_{offset}(IP)}{\Delta z_Q} \propto \frac{\sqrt{\boldsymbol{b}^*\boldsymbol{b}_Q}}{F} \qquad\qquad \text{Eq. 3.14}$$

Here $\boldsymbol{b}_Q$ is the beta function at the quadrupole and F is the focal length of the displaced quadrupole. The maximum offset of the quadrupole that can be corrected with orbit correctors is proportional to this ratio $z_{offset}(IP)/\boldsymbol{D}z_Q$. In Table 3.5 we compare the parameters for the quadrupole where the beta function is the largest.

Tolerances for the LHC quadrupoles were derived in [5]. The rms tolerance for the offset was obtained to be 0.27 mm. Scaling this number by the ratio 2.3/3.1, we obtain a tolerance of 0.2 mm for the VLHC IR quadrupoles. This assumes that corrector strengths similar to those in the LHC (in kick angle) will be used in the VLHC.

Table 3.5. Parameters of the strongest IR quadrupole in the LHC and the VLHC.

Parameter	LHC IR	VLHC (LF) IR
$\boldsymbol{b}^*$ [m]	0.5	0.3
$\boldsymbol{b}_{max}$ [m]	4567	11263
Focal Length, F [m]	21.1	18.7
$z_{offset}(IP)/\boldsymbol{D}z_Q$	~2.3	~3.1

Correctors to correct the orbit at the IP are best placed at 90 degrees from the IP. As in the LHC, correction packages with dipole and skew dipole correction coils should be placed at several high beta locations next to the IR quadrupoles. Spaces between Q2 and Q3 and after Q3 would be ideal locations for these correctors.

IR quadrupole roll angles

Tolerances on the allowed roll angles of the IR quadrupoles may be set by specifying the minimum tune split tolerable before correction. We will assume that this tune split due to roll angles in all sixteen quadrupoles from the two IRs is less than 0.05 before correction. RMS roll angles of 0.5 mrad can be tolerated for the IR quads, assuming that all the IR quadrupole assemblies include a skew quadrupole corrector.

Normally two families of skew quadrupoles are required to correct both the real and imaginary parts of the coupling resonance term. However the phase advance through the IRs is very small and so the imaginary part of the resonance term is negligibly small. Thus only a single skew quadrupole on each side of the IP will suffice to locally correct the coupling in the IR.

Table 3.6 summarizes the misalignment tolerances for the IR quadrupoles. These are based on scaling from tolerances derived for the LHC and should be replaced at a later stage with more exact calculations.

Table 3.6. Misalignment tolerances for the VLHC IR quadrupoles derived by scaling from the LHC IR quadrupole tolerances [5].

Misalignment	Tolerance
Offsets [mm]	0.2
Longitudinal placement [mm]	1
Roll [mrad]	0.5

3.2.3.6   *Crossing Angle*

A crossing angle is required to separate the beams at the parasitic collisions. As is well known, the crossing angle has several effects on the linear and nonlinear optics and beam dynamics, including generation of dispersion due to orbit offsets in the quadrupoles, coupling due to skew multipole errors, and feed down of higher order multipoles. Local dispersion control is required to prevent dispersion waves from propagating into the arcs. This can be performed adjusting pairs of quadrupoles in the cells adjacent to the IRs where there is natural dispersion. A scheme such as this was proposed for the SSC [6]. Correction of local coupling from this and other sources will require skew quadrupoles in the IR as already mentioned. The linear effects from feed-down of higher order multipoles will be corrected by orbit and tune correctors. Nonlinear effects will require nonlinear correction packages in the IRs similar to those in the LHC and RHIC.

3.2.4   **Ground Motion and Emittance Growth**

We have measured the slow ground motion in the 300-ft deep dolomite Conco mine in Aurora, IL, about 3 miles west of Fermilab. The goal of the studies is to record and analyze vertical

ground motion in 8 points separated by 30 meters over a time interval of about 1 year. The experiment in the Aurora mine started in October 2000. The first data reveal that dolomite mine motion is rather small and can be described by the ATL law with coefficient of $A = (6.8 \pm 2.7) \times 10^{-7}$ μm^2/m/s [7]. The resulting maximum orbit distortion in the VLHC which will be caused by this coefficient is of the order of 9 mm/(year)$^{1/2}$.

The only drawback of the Aurora mine experiment is that there are too few sensors, which limits the statistics for studies of spatial correlations. Therefore, a system with about 20 sensors is needed, and long-term measurements should be repeated on a larger scale. Analytical/ computer studies of the slow ground motion effects and orbit correction system and procedures must be performed.

Turn-to-turn dipole magnetic field fluctuations and vibration of quadrupole magnets are of concern, because they can excite coherent beam motion. If the motion is not corrected over the *decoherence time* of about $1/x_{\text{beam-beam}} \approx 1000$ turns, then the coherent motion will be converted into transverse emittance increase and can cause substantial emittance growth over about 10 hours of the store. So far, experimentally measured high-frequency ground or magnet vibrations do not pose a big problem for VLHC [8]. Nevertheless, more detailed analysis on how the lattice may affect the tolerances is needed. For example reference [9] claims that tolerances on vibration amplitude in a lattice with combined function magnets is about 3 times the tolerances in a separated function FODO lattices.

In 1999 experimental studies of high-frequency magnetic field fluctuations were carried out in a Tevatron superconducting dipole magnet. An effective rms dB/B $\approx 10^{-10}$ which is about 10 times the tolerance for the VLHC, was measured. This amplitude could cause emittance doubling after about 6 minutes. The measurements have to be repeated in the VLHC dipole prototypes. Again, we need to analyze and perform computer simulations for lattices with separated and combined function magnets.

Suppression of the emittance growth can be provided by low noise feedback. The first analysis of the FB is presented in [10]. The system has to have sub-micron equivalent input noise. Design and test of such a system at the Tevatron is an important VLHC beam physics R&D task.

3.2.5   Collective Effects

A VLHC Instability Workshop was held at SLAC, March 21-23, 2001 [11]. Most instability issues examined at this workshop are not expected to be serious concerns for the VLHC. Two exceptions are the transverse mode-coupling instability (TMCI) and the transverse resistive wall instability, which are both most pronounced for the Stage-1 collider at injection. In particular, the design intensity of 2.5×10^{10} particles per bunch is a factor of two higher than the expected TMCI threshold. The resistive wall instability will require an extension of the state-of-the-art feedback system. To compensate for the very large incoherent and coherent tune shifts, as well as tune variation along the bunch train due to resistive wall effects, the ring will need to be filled in an appropriate bunch pattern to mitigate this issue.

The rings of both stages have the same size, *2pR* = 233.037 km in circumference, and the same RF frequency. In order to have shorter bunches, the RF frequencies in both phases are chosen 9 times higher than that of the Tevatron, so that the bunches will be separated by 9 RF

buckets. The RF harmonic is $h = 371520$, which is the Tevatron harmonic number scaled to the VLHC circumference.

In the low-field rings, the RF voltage has been chosen to be $V_{rf} = 50$ MV. The rms bunch area of bunches inside the buckets is chosen to be 0.4 eV-sec, the rms bunch area [12] of the Tevatron bunches at 900 GeV. With $V_{rf} = 50$ MV, the maximum energy spread is 2×10^{-3}, and the bucket area is 5 eV-sec. Note that the present Tevatron RF system has a maximum voltage of 1 MV only, thus the bunch length would be too long and the momentum spread too small to fit the higher harmonic buckets at injection. Thus, the Tevatron bunches must be shortened by either a bunch rotation or through the installation of a higher RF voltage before the transfer to the 20 TeV ring is possible.

A bunch excited by forces in the vacuum chamber oscillates in the longitudinal phase space in modes describable by the radial mode parameter n_r designating n_r radial nodes and the azimuthal mode parameter m designating $|m|$ azimuthal nodes. For a given m, the most easily excited radial mode is $n_r = |m|$. Almost distribution independent, the spectrum for the mode designated by $m \neq 0$ peaks at frequency $f(m) » (|m|+1)/2t_L$, where t_L is the *total* length of the bunch in time. For a Gaussian distribution, we approximate it by the 95% length $t_L = 2\sqrt{6}s_\tau$, where s_τ is the rms bunch length. We note that the frequencies for the various VLHC bunch modes of interest are in the GHz range.

3.2.5.1   *Transverse Mode Coupling Instability*

The TMCI threshold for the resistive wall has been calculated in various ways, including analytical formulas, a matrix approach for up to 25 modes, and through particle tracking simulations [11]. The analytic formulas estimate a threshold approximately 40% larger than the matrix approach. The difference between the matrix approach and particle tracking was about 30%. These discrepancies were discussed at the workshop, and future calculations and checks have been planned.

The problem is very important for the low field VLHC. These calculations show that the threshold number for the bunch population at injection with the nominal set of parameters is equal to 1.4×10^{10} protons, about half the nominal intensity. The above estimate assumes a round beam pipe of 9 mm radius. The threshold estimate needs to be redone for the nominal oval-shaped beam pipe.

Assuming that TMCI will exist in the VLHC, the following measures could be a cure:

- Inject low intensity bunches and coalesce them to make high intensity bunches at high field where the TMCI threshold is increased.

- Provide active feedback (resistive damping) at a few low order modes $l = \pm 1, \pm 2, \cdots$

- Introduce an RF quadrupole to provide a tune shift between the head and tail of the bunch.

For this reason, a bunch coalescing scheme has been adopted, which is described in a subsection below. The other two measures will continue to be studied.

The TMCI theory for proton beams is technically challenging because the bunches are longer and other forces may be present. Experimental data for comparison would be most

useful. For instance, it may be possible to study the TMCI using the Tevatron Electron Lens (TEL).

3.2.5.2   Resistive Wall Effects

For the low field ring parameter range the various formulae for the resistive wall impedance agree within a factor of two. The e-folding time for the low frequency resistive wall instability is less than 1 turn. Additionally, the very low revolution frequency leads to a variation in the magnetic image Laslett tune shift when the ring is partially filled during the injection process. The variation is due to the fact that the revolution period is comparable to the magnetic diffusion time through the beam pipe. Initial estimates show a DC tune shift on the order of 0.5 units, with an AC component of about 0.1 units due to the time dependence of the magnetic diffusion into the beam pipe. Increasing the vacuum pipe thickness and/or radius could reduce both of these problems. Increasing the dipole magnet gap can reduce the DC Laslett tune shift, while the variation in tune along the bunch train could be reduced by quadrupoles running at multiples of the revolution frequency. It is envisioned, however, that injecting beam in an appropriately symmetric manner, with bunches entering the ring far apart from each other and gradually filling in between the already injected bunches, the tune variations can be reduced to a tolerable level.

The resistive wall instability needs to be damped. Realistic studies of the feedback system are needed. To fight the transverse resistive wall instability, a fancy feedback system is envisioned [11]. The system would have high-gain, low bandwidth (perhaps 100 kHz) and the pickup signal would arrive at the kicker slightly behind the beam bunch that produced the signal. This feedback system indeed is capable of suppressing the dipole multi-bunch resistive wall growth time of one turn. It is not 100% clear exactly how fast the growth rate is because the theory of resistive wall impedance in this complicated environment (cold, thin coating, magnets outside, etc.) is not easy to calculate. Whether it can suppress beyond one turn is yet to be demonstrated.

3.2.5.3   Bunch Coalescing in the Stage-1 Collider

To alleviate beam instabilities at its injection energy, the Stage-1 collider will have a second RF system for performing bunch coalescing. Five bunches each containing approximately 0.5×10^{10} protons will be coalesced into one bunch of 2.5×10^{10} using a 53.1 MHz system in the Stage-1 collider [13]. If this is performed at 20 TeV, then the 478 MHz system voltage must be reduced from 50 MV to about 6.5 MV and the bunches allowed to rotate 1/4 of a synchrotron period. The main RF system is then turned off, and the second RF system, operating at 53.1 MHz, is snapped on with voltage of 2-3 MV. After 1/4 period in this system, the 53.1 MHz RF is turned back off and the 478 MHz turned on again at approximately 20 MV. The RF voltage is then raised adiabatically to 50 MV completing the process.

This system naturally implies that a 478 MHz RF system be employed at some early stage in the Tevatron injector system. The details of this injector upgrade are yet to be worked out.

3.3　Stage 2 – the High Field Ring

3.3.1　Luminosity versus Energy

The High Field VLHC ring will be the first cryogenic collider to operate in the synchrotron radiation dominated regime, in which the radiation damping time is shorter than the storage time. In this regime there are practical and economic limits to the cryogenic system that can be installed. There is a maximum value P_{cryo} for the synchrotron radiation, which can be absorbed in each ring. It is necessary to adjust the beam parameters to stay within the installed power limit, resulting in an average luminosity that depends on the beam energy E according to a "maximum power law,"

$$L_{ave} < \frac{P_{cryo}}{E}\left(\frac{1}{N_{IP}\boldsymbol{s}_{tot}}\right)\left(\frac{T_0}{T_{store}}\right)$$

Eq. 3.15

Although there is a clear advantage in reducing the storage time, T_{store} must remain significantly larger than the damping time T_0 in order to take advantage of radiatively damped beam sizes. Other factors (such as the refill time) will also play a role in determining the optimum value of T_{store} , but it is safe to estimate that

$$\frac{T_0}{T_{store}} \approx 0.2$$

Eq. 3.16

Except for some uncertainty in this factor, the maximum power law clearly states that the installed capacity to absorb synchrotron radiation at cryogenic temperatures directly limits the attainable product of average luminosity and energy. This trade-off between higher luminosity and higher energy was emphasized in Table 1.2 in Chapter 1.

Similarly, if the beam stored energy per ring $U = NME$ must be kept below a maximum value -- for example if the beam dump has a limited capacity -- then

$$L_{ave} < \frac{U_{max}}{E}\left(\frac{1}{N_{IP}\boldsymbol{s}_{tot}}\right)\left(\frac{1}{T_{store}}\right)$$

Eq. 3.17

Insofar as the stored energy is a practical limit to high field performance -- to the product $L_{ave}E$ -- then there is pressure to reduce T_{store} , and hence to increase the dipole field, to reduce the circumference, and to reduce the refill time.

3.3.2　Operational Performance

For the Design Study, the most straightforward approach is to use as a baseline standard triplet optics and round beams, as in previous hadron colliders. It should be noted, however, that the High Field ring will be the first hadron collider with the potential to take advantage of naturally flat beams. While still under discussion, flat beams are sufficiently new and interesting for hadron colliders that most of the Stage-2 Design Study effort was devoted to analyzing this case up to now. The parameters described below have assumed that the beam emittances evolve into an asymmetric state characterized by $\boldsymbol{k} = \boldsymbol{e}_y/\boldsymbol{e}_x$. The high field ring should be able to achieve $\boldsymbol{k} \ll 0.1$ during a store, consistent with conventional electron storage rings.

Table 3.7. Nominal parameters for stores in the high field ring, using flat beams and doublet IR optics.

Storage energy, E	87.5	TeV
Peak luminosity, L_{max}	2×10^{34}	cm^{-2}sec^{-1}
Collision debris power, per IP	73	kW
Dipole field at storage	9.765	T
Distance from IP to first magnet	30	M
Injection energy	10	TeV
Fill time	30	sec
Acceleration time	2000	sec
Synchrotron radiation damping time, T_0	2.48	hours
Energy loss per turn, U_0	15.3	MeV
Natural transverse emittance (H)	0.0397	μm
Natural RMS momentum width	5.5	10^{-6}
Collision beta horz, $\boldsymbol{b}^*_x$	3.7	m
Collision beta vert, $\boldsymbol{b}^*_y$	0.37	m
Equilibrium emittance ratio, $\boldsymbol{k}$	0.1	
Initial bunch intensity, N	7.5	10^9
Beam current	57.4	mA
Synch. rad. power, per beam, P	.88	MW
Dipole linear heat load	4.7	W/m
Stored energy, per beam, U	3.9	GJ

The instantaneous luminosity is

$$L = \frac{M}{4pT} \frac{N^2 g}{\sqrt{e_x e_y b^*_x b^*_y}}$$

Eq. 3.18

where T is the revolution period. The total number of protons in the ring, MN, is approximately set by the need to provide enough for "luminosity burn-off." Since the number of bunches M is fixed, the need for a given peak luminosity then sets the single bunch population N. Nominal values for these and other parameters, including a conservative value of $\boldsymbol{k} = 0.1$, are given in Table 3.7.

It is the head on beam-beam interaction that sets the minimum horizontal emittance, whether the beams are flat or round. Figure 3.8 shows the horizontal and vertical emittances decreasing to plateau values of $\boldsymbol{e}_x$ and $\boldsymbol{e}_y$ that are consistent with the beam-beam limit, and which are maintained by transverse beam heating. Figure 3.9 shows the corresponding evolution of instantaneous luminosity, and its average, during the store.

3.3.2.1   *The Head-on Beam-beam Interaction*

The horizontal and vertical tune shift parameters for bi-Gaussian round beams ($\boldsymbol{b}^*_x = \boldsymbol{b}^*_y$, $\boldsymbol{e}_x = \boldsymbol{e}_y$) are

$$\boldsymbol{x}_x = \boldsymbol{x}_y = \frac{r}{4p} \frac{N}{\boldsymbol{e}_x}$$
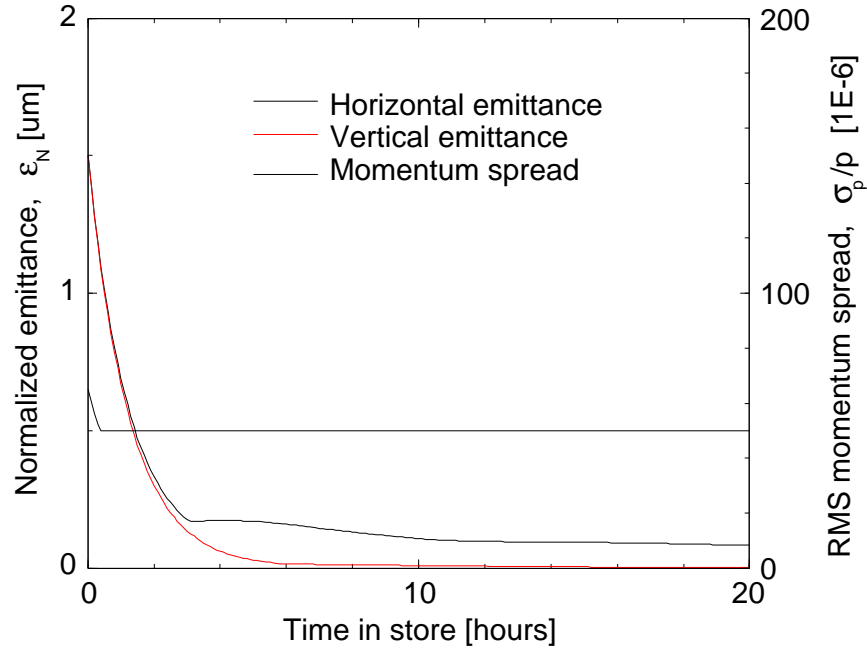
Eq. 3.19

Figure 3.8. Evolution of the transverse emittances and the rms momentum spread during a store.
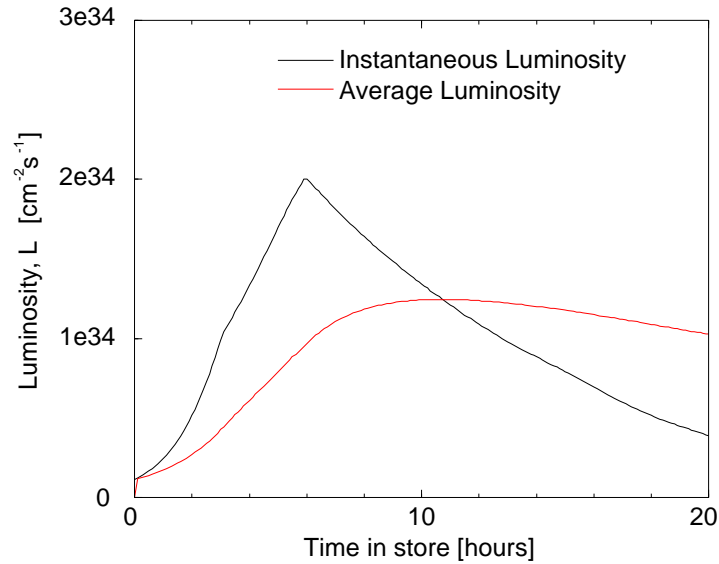

Figure 3.9. Evolution of the instantaneous and average luminosities, during a store.

The beam-beam limit is expected to be approximately the same for round or flat beams, given by

$$x \leq 0.008.$$

This value is justified by practical experience at the SPS and at the Tevatron. The SPS operated at $x \approx 0.004$ (or slightly higher) with 6 collisions per turn. More recently, in Run Ib the Tevatron operated with $x \approx 0.0075$ with only 2 head on collisions per turn (as in the VLHC). Simulations predict that radiation damping might give the high field ring a slight additional advan-

tage, which is by no means as strong as that commonly observed in electron storage rings. The numerical value of 0.008 is illustrated in Figure 3.10, which displays empirical data compiled by Keil and Talman for electron storage rings [14]. The "damping decrement" for the high field VLHC—the fraction of a damping period per head on collision—is approximately 10^{-7}.

Then, re-writing Eqn. 3.18 as

$$L = \frac{M}{4pT} \frac{N^2 g}{ke_x b_x^*}$$

Eq. 3.22

it is explicitly clear that with flat beams the value of b_x^* can be increased by a factor of about $1/k$, significantly simplifying the optics. Equation 3.21 then shows that the value of b_y^* is about the same for flat or round beams.
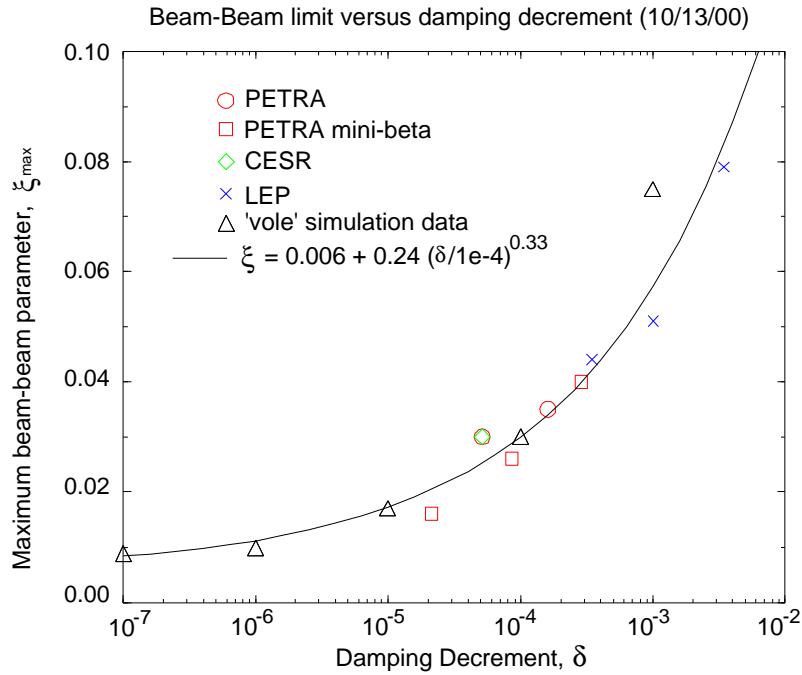

Figure 3.10. Maximum beam-beam parameter vs. damping decrement.

3.3.2.2   Crossing Angles and Parasitic Beam-beam Collisions

The horizontal and vertical tune shifts due to a single parasitic collision are

$$\Delta q_{x,y} \approx \pm \frac{rN}{2pg} \frac{b_{x,y}}{\Delta^2}$$

Eq. 3.23

where the approximation is valid if the full beam separation D is much greater than both horizontal and vertical beam sizes, so that the beam acts like a moving line charge.

If the beams are thoroughly separated (into separate beam pipes, or with very large separations) at a distance L_{sep} from the IP, then there are $4L_{sep}/S_B$ parasitic collisions around each IP, where S_B is the longitudinal bunch separation. The total tune shifts from all parasitic collisions with crossing angle a in one interaction region are

$$\Delta Q_{x,y} \approx \pm \frac{rN}{2pg} \frac{4}{S_B} \frac{L_{sep}}{b^*_{x,y} a^2}$$

Eq. 3.24

where the approximation is most valid if the beams are fully separated before the first IR quadrupole.

Again, assuming one exercises the flat beam option, the horizontal beta function at each collision is much less than the vertical

$$\frac{b_x}{b_y} \approx \frac{b^*_y}{b^*_x} = k$$

Eq. 3.25

so that, taking Eqns 3.24 and 3.25 together gives

$$\Delta Q_x \approx -k \, \Delta Q_y$$

Eq. 3.26

The horizontal tune shift is greatly suppressed with flat beams, to be much smaller than it is with round beams -- if the values of L_{sep} and a compare favorably between the two cases.

3.3.3   Advantages and Disadvantages of Flat Beams

All electron colliders, whether circular or straight, take advantage of flat beams and use doublet optics. However, it has never before been possible to use flat beams in a hadron collider. Flat beams have the advantages and disadvantages discussed below, which continue to be investigated.

Flat beams require the first quadrupole on both sides of the IP to be vertically focusing to both counter-rotating beams (whether the crossing angle is vertical or horizontal). Thus, the optics must be symmetric across the IP, and the first quadrupole must be a 2-in-1 magnet. As seen in the next Section, both optical solutions have been developed.

Table 3.8 compares the performance of flat and round beam in the high field ring. In both cases the beam-beam limit of $x = 0.008$ is reached 5 or 6 hours into the store, when the luminosity is at its peak. The horizontal and vertical emittances values recorded in Table 3.8 are those that are initially maintained (preventing further emittance shrinkage) when the horizontal and vertical beam-beam parameters first saturate. The same peak luminosity is achieved in both flat and round beam cases by adjusting the horizontal and vertical b^* values.

The value of the total crossing angle α is set to be identical with flat or round beams—and is independent of the plane of the crossing angle. The major advantages and disadvantages of flat beams are outlined in the list below:

Flat Beam Advantages
1. Order of magnitude increase of b^*_x, and subsequent reduction of horizontal b_{max} in the doublet quadrupoles. While early separation pushes the first quadrupole further from the IP, the values of b_{max}, both horizontal and vertical, are still reduced, as indicated in Table 3.8.
2. There are far fewer parasitic collisions per interaction region with flat beams than with round beams, greatly reducing the long-range (especially horizontal) tune shift.

Flat Beam Disadvantages

1. The design of the first quadrupole and splitting dipole are difficult. A 2-in-1 quadrupole with relatively close separation will not have as good field quality a single bore element. But, with lower b_{max} in the doublet design, the tolerable field errors are likely to be larger.
2. Neutral particles generated at the IP will aim head-on for the conductor located at the center of the first 2-in-1 quadrupole.
3. Lack of energy flexibility may be a disadvantage to flat beams. At lower energies, damping times are longer and thus flat beams are no longer viable. (However, a lattice has been demonstrated in which 4 IR quadrupoles can act as a doublet or as a triplet [15].)
4. An operational disadvantage is the need for careful tuning to keep the vertical emittance small. Electron rings, however, routinely achieve beam flatness in the range $0.001 < k < 0.01$ by controlling dispersion and global betatron coupling. Flatness values of $k \approx 0.01$ should be achievable.

Table 3.8. Flat and round beam performance parameters after about 6 hours into the store, just after peak luminosity, when both horizontal and vertical beam-beam parameters are saturated.

	FLAT	ROUND
Flatness parameter, k	0.1	1
Beam-beam parameter $x_x = x_y$	0.008	0.008
Peak luminosity L ($10^{34}\,\mathrm{cm^{-2}sec^{-1}}$)	2.0	2.0
Initial bunch intensity $N(10^9)$	7.5	7.5
Collision beta horz b^*_x (m)	3.7	0.71
Collision beta vert b^*_y (m)	0.37	0.71
Maximum beta horz b^*_{max} (km)	7.84	14.58
Maximum beta vert b^*_{max} (km)	10.75	14.58
Horizontal emittance e_x (μm)	0.161	0.082
Vertical emittance e_y (μm)	0.016	0.082
Collision beam size horz s^*_x (μm)	2.53	0.79
Collision beam size vert s^*_y (μm)	0.25	0.79
Maximum beam size horz s^*_{x-max} (μm)	116	113
Maximum beam size vert s^*_{y-max} (μm)	43	113
Total crossing angle a (μrad)	10.0	10.0
Separation distance, L_{sep} (m)	30	120
Number of long range collisions per IR	20	84
Long range tune shift per IR, horz DQ_x	0.0008	0.0166
Long range tune shift per IR, vert DQ_y	0.0081	0.0166

A round beam solution for the VLHC is in hand, including IR magnet designs and optical layouts. Because of the difficult design of a 2-in-1 quadrupole magnet for the doublet optics, the flat beam scenario is at this time a promising upgrade path. The flat beam case with its possible advantages merits further work and discussion and will continue to be studied over the coming months.

3.3.4   Lattice

The lattice geometrically matches the low field (LF) ring lattice so that they both fit in the same tunnel. See Table 3.9 for a selection of HF lattice parameters. The arcs are composed of 90 degree FODO cells using separated function magnets, as are the dispersion suppressors.

3.3.4.1   Triplet IR Optics Approach

Using interaction region optics standard in modern hadron colliders, collisions are created using anti-symmetric triplets for the final focusing. The "round beam" model discussed here is qualitatively similar to the low-field IR design. The triplet quadrupoles are 400 T/m single-bore magnets. Four additional circuits, comprising double-bore 400 T/m magnets are also used for optical matching. With a total of 6 independently-tunable quadrupole circuits available it is possible to match the four b's and a's from the IP into the regular FODO cells, plus hold the phase advance Dm constant across the IR through the squeeze from $b^* = 12.0 \rightarrow 0.50$ m. Fixing Dm eliminates the need for a special phase trombone somewhere in the ring to maintain the nominal operating point. Figure 3.11 shows the lattice functions through the insertion region at collision.

Table 3.9. Short list of some high field lattice parameters.

Horizontal tune	218.19	
Vertical tune	212.18	
Transition gamma	194.13	
Maximum arc beta	459	m
Maximum arc dispersion	1.42	m
Vertical b (store)	0.37	m
Horizontal b (store)	3.7	m
Maximum b, injection	0.61	km
Maximum Horz b, store	7.84	km
Maximum Vert b, store	10.75	km

The circulating beams are separated vertically everywhere in the ring, except in the triplet quadrupoles. Four 10 T dipoles between the Q3 and Q4 quadrupoles bring the beams together at the entrance to the triplet for collisions at the IP. Dipoles downstream of the IP separate the beams again vertically and channel them back into the upper and lower rings. A half-crossing angle of 28.8 μr gives $10s$ separation between the beams at the first parasitic crossing 2.823 m downstream of the IP ($e_N = 1.5\,\pi$ μm at 87.5 TeV/c).

3.3.4.2   Doublet IR Optics Approach

Doublet optics are more naturally suited to the flat beams of the high-field ring. The IR gives 30 m free space from the interaction point to the first magnetic element. For the doublet optics, the first magnet encountered is a high field small bore magnet of 16 T field. This can handle the beams until the total separation becomes 8 mm. Then the beams enter a lower field, 12 T, magnet with a larger bore. These beam separation dipoles bend the beam vertically. This crossing region requires that the beam separation at the first quadrupole be 30 mm. With these

dimensions the first quadrupole is limited to 400 T/m gradient. As the beams separate, a higher quadrupole field can be attained with a limit of 600 T/m.
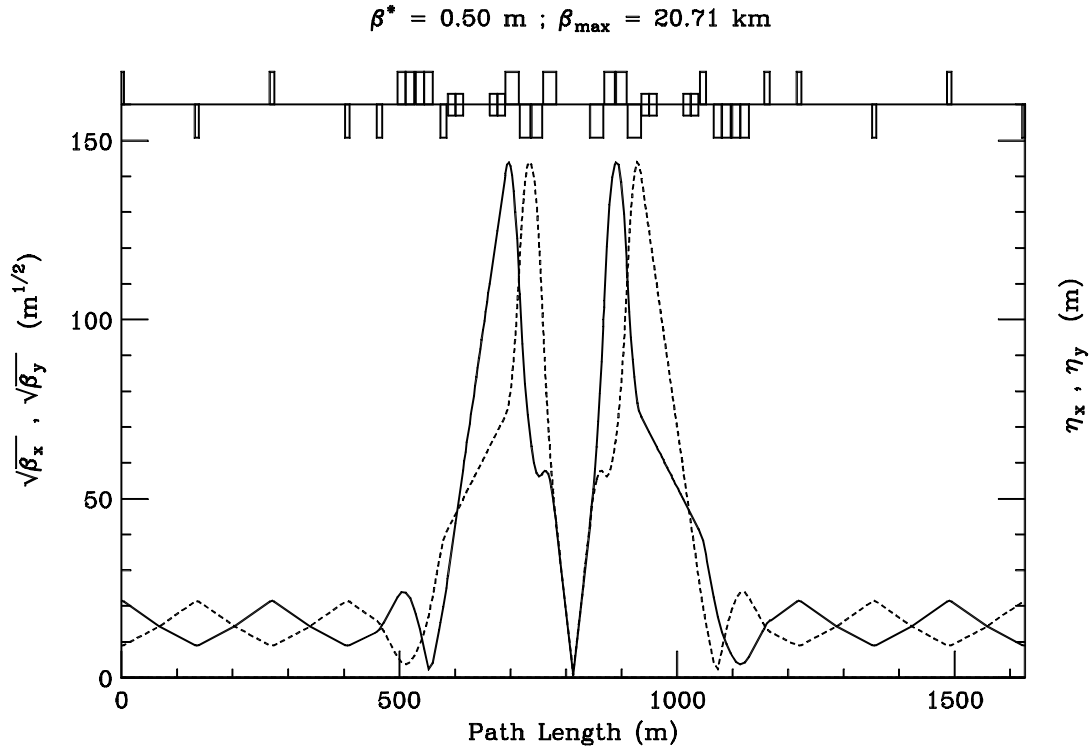

Figure 3.11 Lattice functions near the IP in collision optics, using triplet focusing.

With this design of the crossing region, two interaction regions can fit in the on-site cluster region. The b^* can be varied from 0.37 m to 7.12 m (vertically), b^* horizontally is 10 times larger). The maximum beta is 10.6 km with the collision optics and only about 760 m at injection. Figure 3.12 shows the collision optics of the interaction region.

3.3.5   Magnet Apertures and Field Quality

The effect of the magnetic field quality on the dynamic aperture was investigated at the injection energy of 10 TeV. At injection the beam size has its maximum and errors in the arc magnets dominate the dynamic aperture. With the current one-turn injection scenario, a storage time on the order of seconds is sufficient. To estimate the effect of the magnetic field errors on the single particle dynamic, the nonlinear chromaticity, the tune spread from nonlinear fields and the 1000-turn dynamic aperture were computed. 1000 turns is equivalent to 0.7 seconds real time in the VLHC. Experiments have shown that the dynamic aperture can be computed for storage rings with nonlinear field errors within a 30% error when the field errors are well known [16,17]. For a future machine, however, a larger safety margin is required.
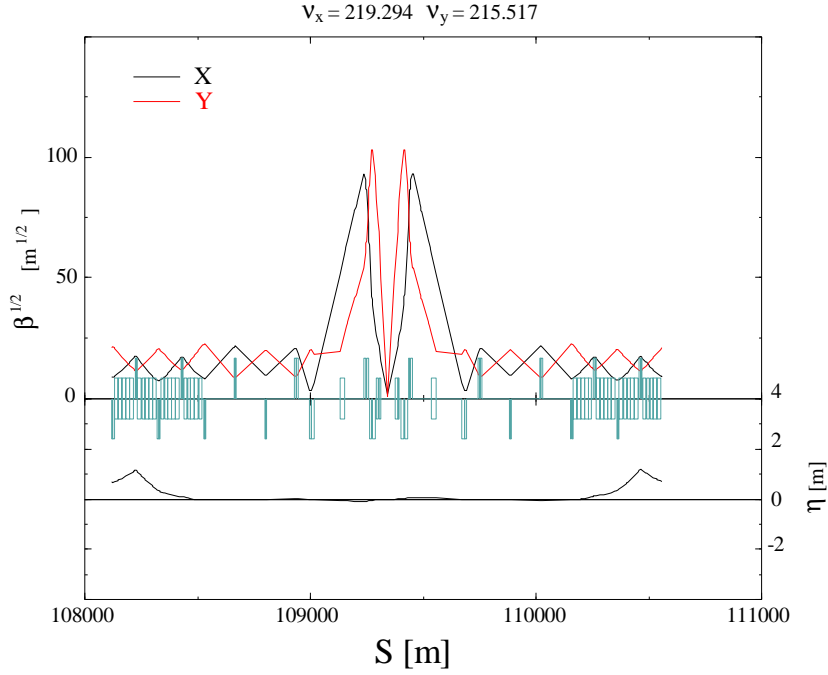
$v_x = 219.294$ $v_y = 215.517$

Figure 3.12. Lattice functions near the IP in collision optics, using doublet focusing.

In the lattice that is used for the evaluation, no interaction regions were inserted since the arcs dominate the dynamic aperture at injection. Arc magnet errors at injection were estimated for a 2.0 T field in the dipoles. The harmonic multipole content used in the simulation is given in Table 3.10. The systematic errors were computed as the maximum possible absolute value with given mean and uncertainties. Random errors were created from a Gaussian distribution, cut at two sigma.

Table 3.10. Systematic <> and random s of multipole coefficients used for Stage-2 tracking at injection. The coefficients are shown in units of 10^{-4} at a reference radius of 10 mm.

Order, n	$<b_n>$	$<a_n>$	$s(b_n)$	$s(a_n)$
1	0.000	0.000	1.20	1.20
2	-2.000	0.000	0.85	0.85
3	0.000	0.000	0.35	0.35
4	0.500	0.000	0.12	0.12
5	-0.006	0.000	0.05	0.05
6	-0.004	0.000	0.02	0.02

Quadrupoles were horizontally and vertically displaced randomly with a Gaussian distribution with a 0.3 mm rms value, cut at three sigma. In addition, beam position monitors were displaced with a 0.2 mm rms value. The resulting non-zero closed orbit was corrected to zero in the beam position monitors with horizontal orbit correctors at focusing quadrupoles and vertical orbit correctors at defocusing quadrupoles. Skew quadrupole errors in the arcs were disregarded and no coupling correction was necessary. The transverse tunes were set to (218.190, 212.180). Both horizontal and vertical chromaticities were set to 2.

No synchrotron motion was included but particles had a relative momentum deviation of $Dp/p = 7.2 \times 10^{-4}$, corresponding to three times the rms of the momentum distribution. The physical aperture of 10 mm in the arcs corresponds to $35s$ of the transverse beam size in the quadrupoles. Figure 3.13 shows dynamic aperture averaged over 10 seeds along with the minimum of the 10 seeds. The error bars of the average dynamic aperture are the rms value of 10 seeds.

Although linear coupling and synchrotron motion were disregarded in the determination of the dynamic aperture, the field quality with the magnet field errors used is sufficient for injection. At collision, we expect the dynamic aperture to be determined by the errors in the IR quadrupoles. Detailed modeling remains to be performed.
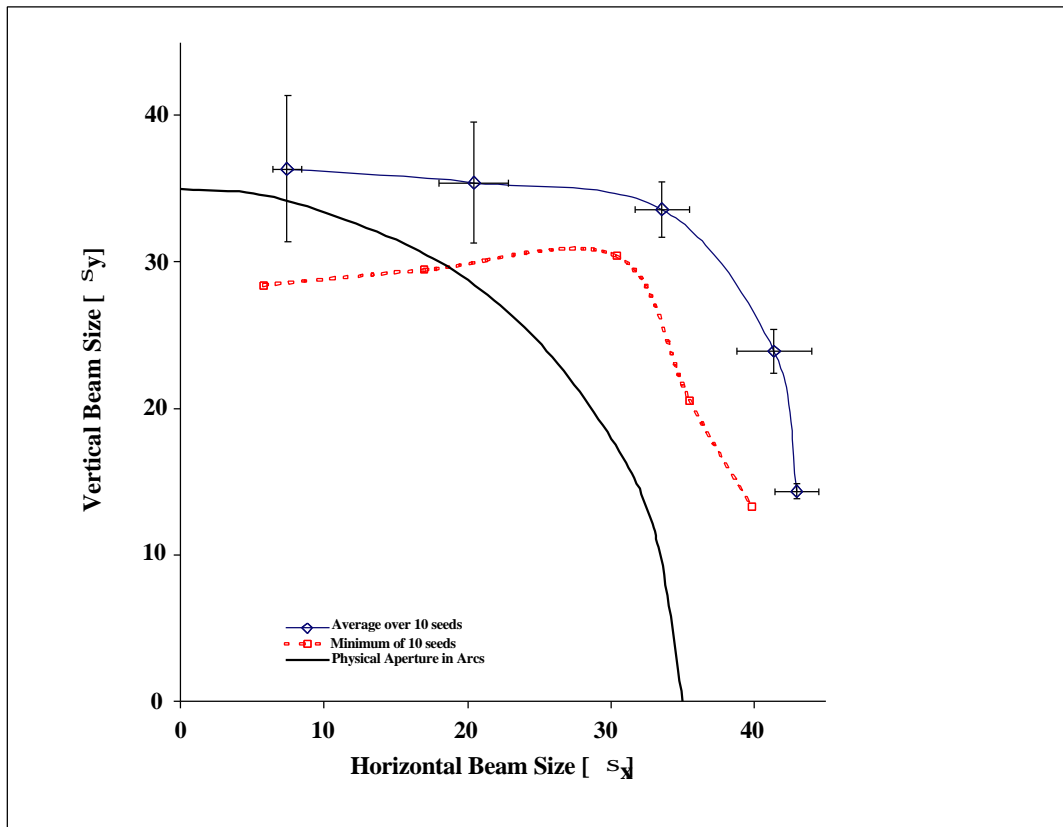

Figure 3.13. 1000-turn dynamic aperture at injection. Shown are the average and minimum over 10 seeds, and the physical aperture, all in units of the transverse rms beam size.

3.3.6   Tolerances and Corrections

In this section we consider the effect of magnet misalignments as well as the effect of main dipole and quadrupole field errors on the beam orbit and betatron tunes. We discuss the tolerances for misalignment and field errors listed in Table 3.11. To this purpose we use the high-field storage optics with $b^*_x = 3.7$ m and $b^*_y = 0.37$ m.

Table 3.11. Tolerance summary for magnet alignment.

RMS ERROR	ARC	IR	
QUADRUPOLES			
Transverse offset	0.25	0.2	mm
BPM to quad offset	0.15	0.1	mm
Roll	0.5	0.5	mrad
Field Error *DK/K*	0.5	0.5	10^{-3}
DIPOLES			
Roll	0.5	0.5	mrad
Field Error *DB/B*	0.5	0.5	10^{-3}

3.3.6.1   *Orbit Errors*

Possible sources of orbit error include transverse quadrupole misalignments (in both the horizontal and vertical directions), main dipole field integral errors (for the horizontal orbit), and roll of the main dipole magnets (for the vertical orbit). In order to estimate and compare the value of the orbit distortion coming from these different types of error sources, the rms closed orbit has been calculated. The calculations assumed the rms magnet misalignments listed in Table 3.11. Each of five different individual perturbation sources were considered in turn. In some cases the errors are introduced in all magnets in the accelerator arcs, while in others the errors are applied to the quadrupoles of one of the interaction region doublets. In the interaction region doublets there is one corrector per plane. The biggest effect comes from quadrupole offsets. The dipole integral field error and dipole roll errors quoted in Table 3.11 have little influence on the required corrector strength.

3.3.6.2   *Tune Error, Coupling and IR Chromatic Effects*

The betatron tune shift caused by an rms quadrupole field error of 10^{-4} and the betatron coupling effect produced by rms quadrupole rolls of 1 mrad have been calculated. The tolerance for arc quadrupole error can be put at 5×10^{-4} providing a 2.5 rms beta-beating value of about 9% is acceptable. A small number of quadrupole correctors placed in the arcs will easily compensate for this beta-beating. Field errors in interaction region quadrupoles can be corrected by adjusting the currents of power supply for these quads. After the current adjustment is done the current fluctuations should be kept well below the 10^{-4} level. Both global correction in the arcs and local skew quadrupole correction in the interaction regions are required for the compensation of betatron coupling effects. With these correction systems in place it is possible to relax the quad roll tolerances to about 0.5 mrad.

Because of the very large maximum *b* values in the interaction region quadrupoles, the chromatic effects produced by these quadrupoles have been evaluated. For the design value of rms momentum spread of 5×10^{-5} the amplitude of the chromatic vertical beta-wave was found to be just a few percent. Thus the effect is not large, mainly due to the small rms momentum spread. The vertical chromaticity produced by the quadrupoles from one interaction region has been found to be about -42. The horizontal chromatic effects are smaller than the vertical.

3.3.6.3   *Corrector Strengths*

The maximum dipole corrector strengths displayed in Table 3.12 are 2.5 times the rms value when all error sources are combined in quadrature. Assuming a maximum achievable field of 3.5 T for the IR dipole correctors, and 2.2 T for the arc dipole correctors, magnetic lengths of 1.05 m in the arcs and 2.5 m in the IRs are required. If the maximum corrector strengths are increased to higher values than those cited in Table 3.12 then the corresponding tolerances in Table 3.11 can be relaxed accordingly.

Even the maximum dipole corrector strengths listed in Table 3.12 cannot make up for the magnet alignment diffusion caused by ground motion. Ground motion might put magnet offsets well beyond the defined tolerances after a few years of movement. Thus, periodic magnet realignment will be necessary. Some means to simplify the realignment procedure, such as using stepping motors, should be evaluated.

Table 3.12. Corrector magnetic lengths and strengths. The maximum strengths are 2.5 times the rms value required when all contributions are added in quadrature.

ARC CORRECTORS		
Dipole magnetic length	1.05	m
Dipole max strength	2.3	T-m
Skew quad length	0.95	m
Skew quad max strength	95	T
Sextupole magnetic length	0.95	m
Sextupole max strength, $L(d^2B/dx^2)$	7400	T/m
IR CORRECTORS		
Magnetic length	2.5	m
Dipole max strength	8.6	T-m
Skew quad max strength	95	T

3.3.7   Collective Effects

The reduced bunch population and higher energy of the Stage-2 collider greatly diminish the instability issues found in the Stage-1 collider. While uncertainties of the transverse impedance are larger for the high field ring, worst case estimates lead to resistive wall e-folding times of order 3 turns, significantly slower than in the low field case. Any damper technology required should easily follow from that developed for the low field case. Future studies may indicate that increasing the thickness of the copper layer is beneficial for reducing any resistive wall effects. The effect of dipole magnetic fields on the resistivity of the various materials used in the high field design needs to be well understood.

References

[1]   David Neuffer, *Particle Accelerators* **23** (1988), 21.

[2]   F. Ostiguy, personal communication, March 19, 2001.

[3]   G. Ambrosio, personal communication, March 22, 2001.

[4]   T. Sen et al, "Chromaticity Correction for the SSC Collider Rings," *Proc. 1993 IEEE Part. Accel. Conf*, 143 (1993).

[5]   T. Sen, "Alignment tolerances of IR quadrupoles in the LHC," FNAL-Conf-99-304 (October 1999).

[6]   Y. Nosochkov and D. Ritson, "Provision of IP crossing angles for the SSC," SSCL-Preprint-367 (1993).

[7]   V. Shiltsev, *Proc. ICFA Workshop on Ground Motion*, Nov. 2000, SLAC; http://www-project.slac.stanford.edu/ls/wkshp/GM2000.

[8]   B. Baklakov et al., *PRST Accel. Beams*, 031001, 1998.

[9]   V. Shiltsev, FNAL TM-1987, 1996.

[10] A. Burov et al., "Beam Stability Issues in a Very Large Hadron Collider," *NIMA* 450, p. 194, 2000.

[11] Workshop information and presentations can be found at http://www.slac.stanford.edu/~achao/VLHCworkshop.html.

[12] See for example, K.Y. Ng, "Impedances and Collective instabilities of the Tevatron at Run II," Fermilab Report TM-2055, 1998.

[13] K.Y. Ng, "Bunch Coalescence in Low-Field VLHC Rings," report in progress (April 2001).

[14] E. Keil, R. Talman, "Scaling of Luminosity Data Between e^+e^- Storage Rings," *Particle Accelerators,* Vol. 14 pp. 109-118, 1983.

[15] S. Peggs, M. Harrison, F. Pilat, M. Syphers, "Flat beams in a 50 TeV hadron collider," Vancouver PAC 97, 1997.

[16] W. Fischer, *An Experimental Study on the Long-term Stability of Particle Motion in Hadron Storage Rings*, Ph.D. thesis, Hamburg University, DESY 95-235 (1995) and CERN SL/96-10 (AP), 1996.

[17] W. Fischer, M. Giovannozzi and F. Schmidt, "Dynamic Aperture Experiment at a Synchrotron," *Phys. Rev. E*, Vol. 55, Number 3, p. 3507, 1997.